Dynamic regimes and bifurcations in a model of actin-based motility

Mihaela Enculescu,[1] Azam Gholami,[2] and Martin Falcke[1]

[1]*Department of Theoretical Physics, Hahn-Meitner-Institute, Glienicker Strasse 100, 14109 Berlin, Germany*

[2]*Department of Fluid Dynamics, Pattern Formation and Nanobiocomplexity, Max-Planck-Institute for Dynamics and Self-Organization,*
Am Faßberg 11, 37077 Göttingen, Germany

Propulsion by actin polymerization is widely used in cell motility. Here, we investigate a model of the brush range of an actin gel close to a propelled object, describing the force generation and the dynamics of the propagation velocity. We find transitions between stable steady states and relaxation oscillations when the attachment rate of actin filaments to the obstacle is varied. The oscillations set in at small values of the attachment rate via a homoclinic bifurcation. A second transition from a stable steady state to relaxation oscillations, found for higher values of the attachment rate, occurs via a supercritical Hopf bifurcation. The behavior of the model near the second transition is similar that of a system undergoing a canard explosion. Consequently, we observe excitable dynamics also. The model further exhibits bistability between stationary states or stationary states and limit cycles. Therefore, the brush of actin filament ends appears to have a much richer dynamics than was assumed until now.

PACS number(s): 87.15.−v, 05.45.−a, 87.16.−b, 87.17.Aa

I. INTRODUCTION

Cell motility is essential in life. During morphogenesis, dividing cells of an organism move in a controlled way to sites where they form specific tissues and organs. Cells of the immune system move to the place of an infection to kill the microorganisms causing it. Connective tissue cells move to a wound place to replace the damaged units when a wound is healing. In most cases, the cytoskeleton of the cell plays the essential role in generating the forces driving cellular motility [1,2]. The cytoskeleton is a cross-linked branched network of biopolymers of different stiffness. Among them, semiflexible actin filaments have the remarkable property of being polarized, with one end growing by polymerization and the other end shrinking by depolymerization. Actin filaments organize with their growing ends oriented toward the intracellular obstacle, for example, the cell membrane, as a response to external stimuli. The self-assembly mechanism is still the subject of intensive research [3]. Polymerization of the actin filaments against the obstacle creates a mechanical stress that pushes it forward [4–6]. Depolymerization at the opposite end of the filaments perpetuates the force-generating process by releasing actin monomers that diffuse to the front, where they are consumed by polymerization [2].

Several pathogens, such as *Listeria monocytogenes*, use the host cell's actin polymerization machinery to propel themselves through the host cell or even to cross to neighboring cells [7]. The surface of the bacterium contains the protein ActA, which induces the assembly of free actin into a cometlike tail of cross-linked filaments oriented with their rapidly polymerizing ends toward the posterior end of the bacterium [8,9].

While the motion of the wild-type *Listeria* is steady, the intracellular movement of its mutant expressing ActA-Δ_{21-97} is oscillatory and shows a particularly interesting temporal pattern [10,11]: the bacterium moves very slowly over a period of time varying between 30 and 100 s in different experiments, jumps forward during the next several seconds,

and then slows down again abruptly. Such periodic solutions, consisting of long intervals of slowly changing dynamics that alternate with short periods of very fast transition, are found in several chemical and biological systems and are known as relaxation oscillations [12]. The existence of such abrupt changes in the temporal behavior of the system (e.g., Fig. 8 in [11]) suggests the presence of certain dynamical properties, such as excitability and sudden transitions from steady to oscillatory solutions. Awareness of these dynamic regimes could be important for understanding more complex spatiotemporal phenomena found for actin-based motility [13–15]. As a first step, we analyze here a mathematical model for actin-based motility and focus on these dynamic properties and their mathematical background.

Actin-based propulsion can be reconstituted *in vitro* using plastic beads, lipid vesicles, and oil droplets [16–18]. Experiments on ActA-coated beads and vesicles have revealed a similar hopping movement. These systems have the advantage of providing access to experimental parameters. Variation of the bead diameter and the surface density of protein caused transitions from saltatory motion to a steady regime, like the smooth movement of the wild-type *Listeria* [18].

The actin-based propulsion of *Listeria monocytogenes* was modeled at a mesoscopic level [11] by treating the actin tail as a continuous elastic gel. The model exhibits both steady and saltatory motion. Saltatory motion arises from a stick-slip transition caused by nonlinear friction between the gel and the moving obstacle. That requires curved surfaces for hopping to occur. Furthermore, the model predicts that the strength of the linkage between *Listeria* and the actin tail is stronger during the slow phase and weaker during the rapid one. Recently, an alternative microscopic model for *Listeria* propulsion was proposed [19], which focuses on the details of the force generation process and the balance between the pulling forces exerted by actin filaments bound to the surface of the bacterium, and the pushing forces of the polymerizing actin filaments. This approach also reproduces the two regimes of motion observed in experiments. Saltatory motion arises from a push-pull mechanism and does not
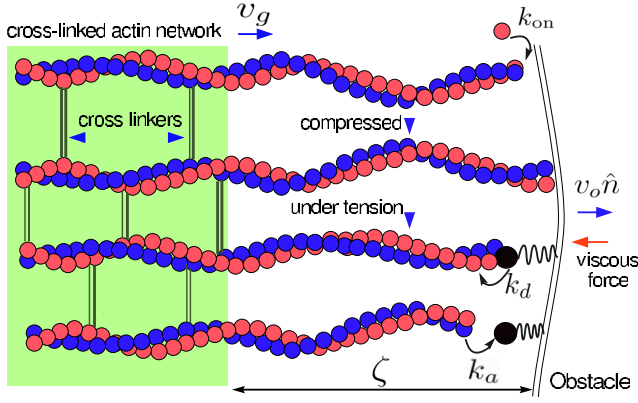
FIG. 1. (Color online) Schematic representation of the model: Polymers are anchored with one end into a cross-linked network and oriented with the other end against an obstacle. Filaments can attach to the surface of the obstacle at rate k_a. Attached polymers can detach again at rate k_d. Detached filaments polymerize at rate k_{on}. The boundary of the cross-linked network advances with velocity v_g. The obstacle moves with velocity v_0 into a viscous medium.

require bent surfaces. The model predicts that the increase of the rate at which actin filaments attach to the surface of the bacterium can induce a transition from the steady to the periodic regime. Further increase of this parameter induces a second transition from the oscillatory to the steady regime.

The present paper focuses on the transitions between the oscillatory and steady regimes in this model [19]. We show that the initiation of the relaxation oscillation at the first transition is due to a homoclinic bifurcation. Slightly inside the oscillatory regime, a stable limit cycle coexists with one stable and two unstable stationary states. The stable steady state is far from the limit cycle, which is located near the unstable ones. At the transition point, the limit cycle collides with one of the unstable points, and a trajectory ending in the stable steady state emerges. The second transition is due to a Hopf bifurcation of the steady state followed by a sudden explosion of the stable Hopf cycle with small amplitude and small period into large relaxation oscillations with big amplitude and big period. The transition is preceded by excitability of the stable state: Even small perturbations cause the system to make a very large amplitude excursion before returning to the steady state. The trajectory during such an excursion follows part of the big limit cycle found after the transition.

II. DESCRIPTION OF THE MODEL

We describe here the microscopic model of actin-based propulsion developed in [19]. We assume a population of $N \approx 200$ parallel actin filaments oriented with their fast-growing ends toward an obstacle (see Fig. 1). In this paper we consider the case of polymers normal to the obstacle, which are allowed to fluctuate in three dimensions. Some results on oscillations with tilted filaments and crossed populations are reported in [19]. Filaments may attach to the obstacle by different mechanisms [3,20,21] resulting in a population of attached filaments (number n_a and mean free
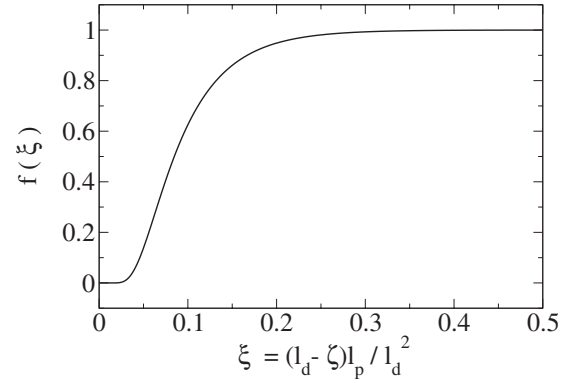

FIG. 2. Scaling function for the entropic force exerted on a wall by a polymer in the semiflexible limit $l_d \ll l_p$.

contour length l_a) and a detached population (number n_d, mean free contour length l_d). Attached filaments can detach with the stress-dependent rate k_d, depending on the force F_a exerted on the obstacle as

$$k_d(F_a) = k_d^0 \exp(-\delta F_a / k_B T),$$

where $\delta \approx 2.7$ nm is the size of an actin monomer and $k_d^0 \approx 0.5$ s^{-1} the detachment rate in the absence of forces [22].

The attachment rate k_a of the polymers can be assumed to be constant in a certain vicinity of the obstacle only. In principle, our detached model filaments could attach even if they are outside that region. However, if they do, they detach immediately again. This behavior follows from the force dependence of the detachment rate k_d, which diverges exponentially with increasing distance. Additionally, typically $l_d > l_a \approx \zeta$ applies and detached filaments with a large distance between obstacle and tip do not occur; the tip of detached filaments is almost all the time at the obstacle and pushes it. Therefore, k_a can be assumed to be constant for all filament positions, without changing the physics of the problem (no attached filaments if the filament tips are too far from the wall). We make this assumption to simplify the numerical handling of the equations, since n_a can now become very small, but does not vanish.

Polymers attach by elastic linker proteins to the surface of the obstacle. The serial arrangement of polymer and linker leads to a piecewise linear force (see [19] for details)

$$F_a(l_a, \zeta) = \begin{cases} -k_{\parallel}(\zeta - R), & \zeta \leq R, \\ -k_{eff}(\zeta - R), & R < \zeta < l_a, \\ -k_l(\zeta - l_a) - k_{eff}(l_a - R), & \zeta \geq l_a, \end{cases}$$

where $R(l_a) = l_a(1 - l_a/2l_p)$ is the equilibrium length of the polymer, $k_{\parallel}(l_a) = 6k_B T l_p^2 / l_a^4$ [23] is the linear response coefficient of a grafted wormlike chain, $k_l \approx 1$ pN/nm denotes the spring constant of the linker, and $k_{eff} = k_l k_{\parallel} / (k_l + k_{\parallel})$ is the effective linear coefficient.

Detached filaments grow with the polymerization velocity v_p, depending on the force F_d with which the polymer pushes against the obstacle as
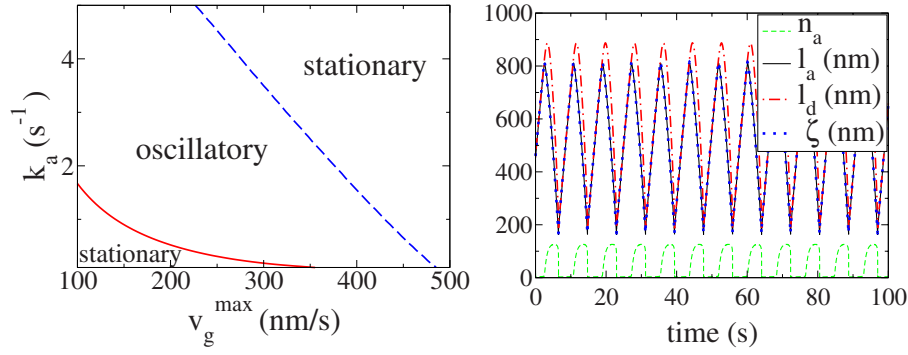
FIG. 3. (Color online) Left: Phase diagram of the model (1) outlining stationary and oscillatory regimes. Right: Oscillatory solution obtained for $v_g^{\max}=300$ nm s^{-1} and $k_a=1$ s^{-1}.

$$v_p(F_d) = v_p^{\max} \exp(-\delta F_d/k_B T),$$

with $v_p^{\max} \approx 500$ nm s^{-1} being the free polymerization velocity [24].

The pushing force F_d of a single detached filament growing against an obstacle is of entropic origin and has been calculated in [25]. It depends on the free contour length l_d of the filament and on the distance ζ to the obstacle in a nonlinear manner. In the semiflexible limit $l_d \ll l_p$, where $l_p \approx 15\ \mu$m denotes the persistence length of the polymer, a scaling law may be obtained for the entropic force [25]. In this regime we have

$$F_d(l_d,\zeta) = \frac{\pi^2 k_B T l_p}{4 l_d^2} f\left(\frac{(l_d - \zeta) l_p}{l_d^2}\right).$$

The scaling function f is shown in Fig. 2.

At the end opposite to the obstacle, filaments are assumed to be anchored into a cross-linked network that advances with the velocity

$$v_g(l) = v_g^{\max} \tanh(l/\bar{l}),$$

depending on the free contour length l of the filament. It is assumed that the cross-linking velocity is proportional to the free contour length for short polymers and saturates to a maximum value for lengths of the order of $\bar{l} \approx 100$ nm.

As shown in [19], the system may be completely described by four dynamic variables: the number n_a of attached filaments, the lengths l_a, l_d of attached and detached filaments, and the distance ζ between the graft point of the filaments and the obstacle. The time evolution of these variables can be computed from the equations governing the length distributions of attached and detached filaments and using a monodisperse approximation (see the Appendix),

$$\partial_t n_a = -k_d n_a + k_a n_d,$$

$$\partial_t l_a = -\max\left(\frac{l_a}{\zeta}, 1\right) v_g(l_a) + k_a \frac{n_d}{n_a}(l_d - l_a),$$

$$\partial_t l_d = v_p - \max\left(\frac{l_d}{\zeta}, 1\right) v_g(l_d) + k_d \frac{n_a}{n_d}(l_a - l_d),$$

$$\partial_t \zeta = \frac{1}{\eta}(n_a F_a + n_d F_d) - \frac{1}{N}[v_g(l_a) n_a + v_g(l_d) n_d], \quad (1)$$

where $n_d = N - n_a$ denotes the number of detached filaments. The obstacle is assumed to move in a medium with an effective viscous coefficient η. For an obstacle of several micrometers length and a medium ten times more viscous than water, η is about 10^{-3} pN s nm^{-1}. The factor $\max(l/\zeta, 1)$ in the equations for l_a and l_d gives the ratio of the polymer contour length swallowed by the growing network to the distance it advances in the direction normal to the obstacle. That factor is equal to 1 when the polymer is stretched ($l < \zeta$) and to l/ζ when the polymer is bent ($l > \zeta$).
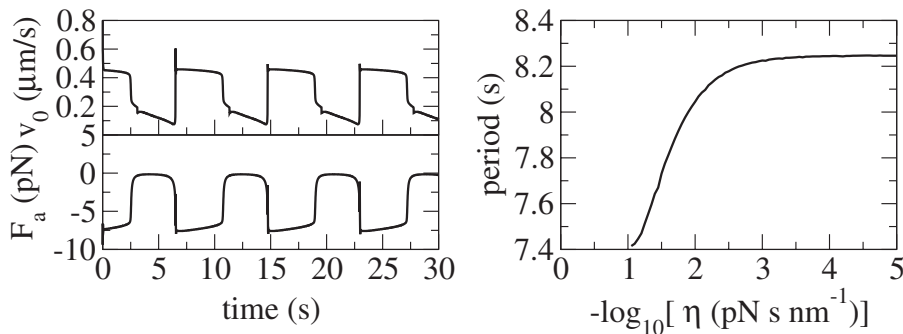

FIG. 4. Left: Time evolution of the obstacle velocity v_0 and of the force F_a during the oscillation in Fig. 3. Right: Saturation of the period of the cycle to a bounded nonzero limit value when the viscous coefficient η is decreased from 10^{-1} to 10^{-5} pN s nm^{-1}.
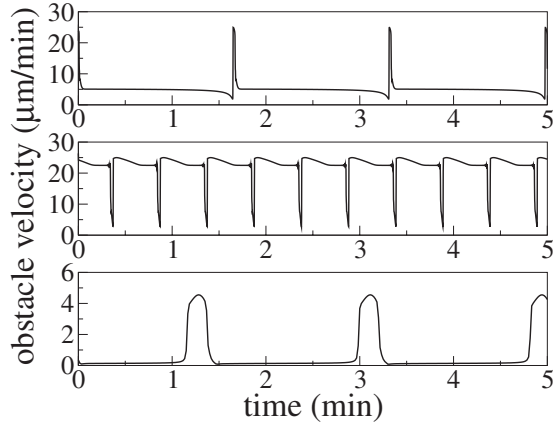
FIG. 5. Different oscillation patterns obtained when the parameters are varied. Variation of v_g^{max} changes the ratio between the durations of the fast and slow phases: Close to the lower transition (top panel: $v_p^{max}=300$ nm s^{-1}, $k_d=0.5$ s^{-1}, $k_a=2$ s^{-1}, $v_g^{max}=85$ nm s^{-1}), the obstacle moves slowly most of the time and makes short jumps periodically, similar to the movement of *Listeria*. Close to the upper transition (middle panel: $v_p^{max}=300$ nm s^{-1}, $k_d=0.5$ s^{-1}, $k_a=2$ s^{-1}, $v_g^{max}=375$ nm s^{-1}), the obstacle moves fast most of the time and makes short breaks periodically. The height of the velocity peaks is influenced mainly by the free polymerization speed v_p^{max}. Bottom panel ($v_p^{max}=150$ nm s^{-1}, $k_d=0.2$ s^{-1}, $k_a=1.8$ s^{-1}, $v_g^{max}=50$ nm s^{-1}) shows oscillations comparable to the movement of oil droplets (see [27], Fig. 3).

III. OSCILLATIONS

Numerical simulations of the time evolution of the model when the attachment rate k_a and the maximal graft velocity v_g^{max} are varied lead to the phase diagram in Fig. 3 (left panel): There is an oscillatory regime, separated from the steady state regime by two transition lines. Note that the lower transition line is tangent to $k_a=0$, so that there are no oscillations if there is no attachment of the filaments to the surface of the obstacle. Oscillations are, however, possible for very small values of the attachment rate and $v_g^{max} \lesssim v_p^{max}$. Figure 3 (right panel) shows an example of the simulation results for a set of parameters inside the oscillatory regime: The system switches periodically and in a very short time between a state with a high ratio of attached polymers, characterized by slowly decreasing lengths of attached and detached filaments, and a state with almost no attached poly-

mers and slowly increasing polymer lengths. The plots of the velocity v_0 of the obstacle and of the force F_a show the characteristic form of a relaxation oscillation, with short periods of very fast transition alternating with long periods of slow dynamics (see left panel in Fig. 4). This periodic structure is typical for systems having at least one component that changes very fast compared to the other variables. The induction of such a separation of time scales in our system is twofold: first, by the relatively small value of the viscous coefficient η, and, second, by the particular form of the balance between the polymerization force $n_d F_d$ and the force exerted by bound filaments, $n_a F_a$ [26]. If the obstacle is in equilibrium ($\partial_t \zeta=0$), these two forces have almost equal size but opposite signs, such that $|n_a F_a + n_d F_d| \ll |n_a F_a| \approx |n_d F_d|$; although already small perturbations of this balance result in a very big cumulative force, which tries to reestablish it again. As expected for relaxation oscillations, when η is decreased by several orders of magnitude, the period of the cycle converges to a bounded nonzero limit value (see right panel in Fig. 4). For further discussion of the fast and slow dynamic variables, see Sec. IV. In the whole oscillatory regime, the cycle shows two alternating phases. The first one is characterized by high obstacle velocity, increasing filament lengths, and a small fraction of attached polymers. By contrast, during the second phase the obstacle moves slowly, filament length decreases, and the fraction of attached polymers is high. The lengths of the two oscillation phases and their ratio vary, however, inside the oscillatory regime (see Fig. 5). Oscillations with a fast phase considerably shorter than the slow phase can be obtained especially near the lower border of the oscillatory regime (see Fig. 5, top panel, and also next section). They exhibit periodic spikelike maxima of the obstacle velocity. For a detailed discussion of this type of oscillation, which is relevant for the modeling of the hopping *Listeria*, see [19]. The fast phase represents a larger fraction of the period with oil droplets propelled by actin polymerization [27], similar to the example in Fig. 5, bottom panel.

In this paper we go beyond these regimes and discuss the whole parameter domain that may be relevant for other biological systems which exhibit actin-based motility. In particular, a thorough understanding of the local dynamics is a prerequisite for understanding spatiotemporal phenomena.

IV. HOMOCLINIC BIFURCATION

Deep inside the oscillatory regime shown in Fig. 3, oscillations set in independent of the chosen initial conditions of
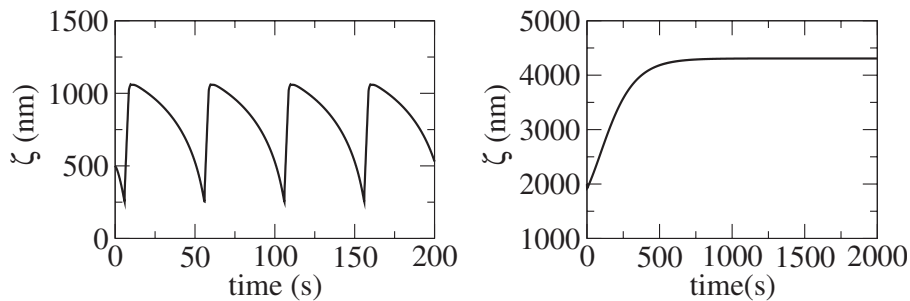

FIG. 6. Numerical simulations of Eq. (1) for a set of parameters ($v_g^{max}=200$ nm s^{-1} and $k_a=0.55$ s^{-1}) where the system shows bistability. Depending on the initial conditions, the system reaches a stable limit cycle (left case) or a stable steady state (right case). Note that the steady state is far away from the limit cycle.
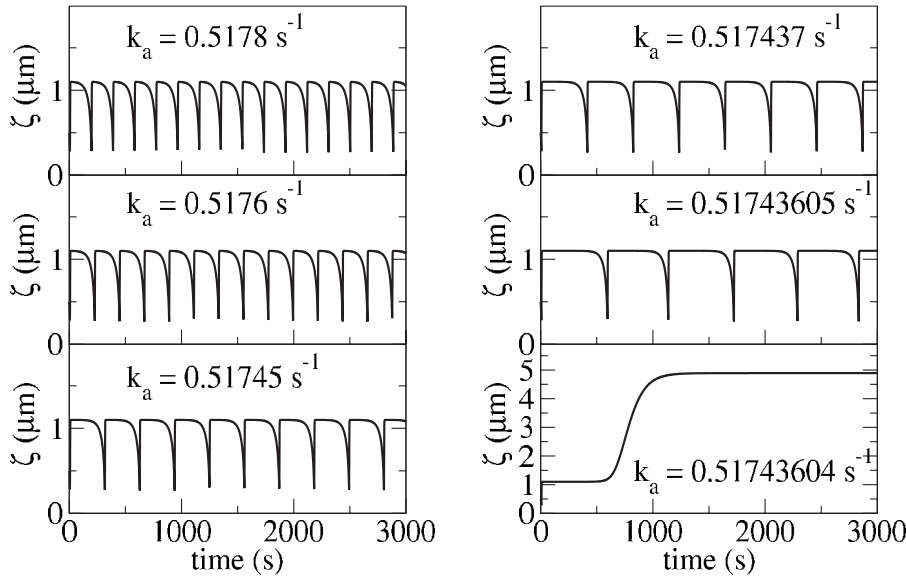
FIG. 7. Evolution of the system when the lower transition line is crossed from above for $v_g^{max}=200$ nm s^{-1}. When the transition is approached, the period of the relaxation oscillations diverges within a short parameter interval; the amplitude remains constant. Note the different scaling of the ζ axis after the transition (last panel).

the simulations. However, if we start in this regime and slowly reduce the attachment rate, we find just before the lower transition line coexistence of the stable limit cycle with a stable steady state, which is situated far away from the limit cycle in phase space. Depending on the initial values, either oscillations or the steady state is reached, as shown in Fig. 6 (see also Sec. VI). When the limit cycle is selected by the initial condition, we find that its period increases very fast on approaching the lower transition line, while its amplitude remains unchanged. At the transition, oscillations disappear with finite amplitude, and the stable steady state, which was present also before the transition, remains as an attractor only (see Fig. 7). Direct computation of the steady states by imposing stationarity in Eq. (1) and linear stability analysis leads to the following scenario (see Fig. 8). Deep inside the oscillatory regime, there exists only one unstable steady state; when the lower transition line is approached from above, two new steady states appear via a saddle-node bifurcation (*A*). Therefore, between the saddle-node bifurcation line and the lower transition line, a stable steady state coexists with the stable limit cycle and two other unstable steady states. The stable steady state is far from the limit cycle, which is located around the lower unstable state and below the upper unstable state. When the transition line is crossed, the limit cycle collides with the upper unstable point in a homoclinic bifurcation (point *D*) and the system is attracted by the only existing stable steady state. When the attachment rate is further decreased, the lower unstable state becomes stable via a Hopf bifurcation (*C*) and disappears shortly after by colliding with the remaining unstable state (point *B*). The limit cycle arising from the Hopf bifurcation in point *C* has a tiny amplitude and disappears between *C* and point *D* in a bifurcation which we did not investigate in detail.

V. CANARD EXPLOSION AND EXCITABILITY

The sudden growth of the amplitude and period of a limit cycle over a short parameter interval is known as canard explosion [12]. Canard explosions have been evidenced experimentally in several chemical systems subject to relaxation oscillations, such as the Belousov-Zhabotinski reaction or gas-phase reactions such as hydrogen oxidation [28,29]. Canard explosion and excitability are closely linked, as discussed previously [30]. Both phenomena are present in our system when the upper transition line is crossed. When started very close to the steady state, numerical simulations show first the presence of a supercritical Hopf bifurcation (confirmed by the linear stability analysis), and the explosion
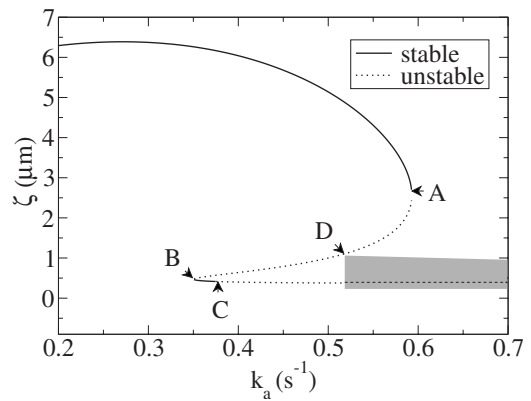

FIG. 8. Dependence of the steady states of the system and their linear stability on the attachment rate k_a near the lower transition for $v_g^{max}=200$ nm s^{-1}. The shaded area represents the states on the limit cycle. The following transitions are displayed: saddle-node bifurcations (*A* and *B*), Hopf bifurcation (*C*), and homoclinic bifurcation (*D*).
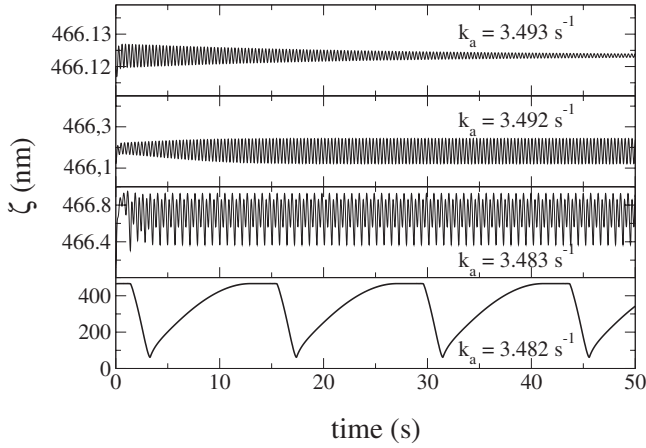
FIG. 9. Evolution of the system when the upper transition line is crossed from above at $v_g^{max} = 300$ nm s^{-1}. First, the steady state loses stability via a supercritical Hopf bifurcation; a stable limit cycle with small amplitude and small period appears. Shortly after, the limit cycle explodes into big relaxation oscillations. Note the different scaling of the panels.

of the small Hopf cycle to large relaxation oscillations nearby in parameter space (see Fig. 9). If the initial condition is slightly perturbed, the system shows excitability before the transition to big amplitude oscillations (Fig. 10).

The analysis of the trajectory shows a strong correlation of the length variables l_a and l_d and ζ. In order to identify the basic dynamic variables of the system, we perform therefore a coordinate transformation, replacing l_d and ζ by the differences $x := l_d - l_a$ and $y := \zeta - l_a$. Furthermore, we reduce the system by making the pseudo-steady-state approximation for n_a. Setting $\partial_t n_a = 0$ and inserting the solution

$$n_a(l_a, y) = n \frac{k_a}{k_a + k_d(l_a, y)}$$

into the remaining three equations, we obtain a system of the form

$$\partial_t l_a = f_1(l_a, x, y; k_a),$$

$$\partial_t x = f_2(l_a, x, y; k_a),$$

$$\eta \partial_t y = f_3(l_a, x, y; k_a, \eta). \tag{2}$$

Numerical simulations of (2) show qualitatively the same behavior as the full system when going from large to small values of k_a. For $k_a > k_a^H(\eta)$, a stable steady state exists. It loses stability by a Hopf bifurcation at $k_a = k_a^H(\eta)$. At $k_a = k_a^C(\eta)$ with $k_a^C < k_a^H$, the small limit cycle explodes into big relaxation oscillations.

Due to the small value of the viscosity η of the intracellular fluid, the variable y induces a fast time scale $\tau := t/\eta$. The dynamics of (2) can also be explained theoretically for $\eta \ll 1$ [12] by analysis and combination of the dynamics of the *reduced problem*

$$0 = f_3(l_a, x, y; k_a; 0),$$

$$\partial_t l_a = f_1(l_a, x, y; k_a),$$

$$\partial_t x = f_2(l_a, x, y; k_a),$$

and the dynamics of the *layer problem*

$$\partial_\tau y = f_3(l_a, x, y; k_a, 0),$$

$$\partial_\tau l_a = 0,$$

$$\partial_\tau x = 0.$$

System (2) has the following remarkable properties [compare conditions (A1) and (A4) (A3′) (A4′) in [12]].

(I) The critical manifold $M := \{(l_a, x, y) : f_3(l_a, x, y; k_a, 0) = 0\}$ is folded; the plane sections through M for constant values of x are S shaped (see Figs. 11 and 12).

(II) For the layer problem, the upper and lower branches are attracting ($\partial f_3 / \partial y < 0$) and the middle branch is repelling ($\partial f_3 / \partial y > 0$). Therefore, when started away from the critical surface M, the system will move rapidly to one of the attracting branches.

(III) For $k_a \leq k_a^C(0)$, the slow flow on M satisfies $\partial_t l_a > 0$ on the upper branch and $\partial_t l_a < 0$ on the lower branch. This ensures that the system, once it has reached an attracting branch, moves always toward the fold.

(IV) For $k_a \neq k_a^C$, the two folds $F := \{(l_a, x, y) \in M : \partial f_3 / \partial y (l_a, x, y; k_a, 0) = 0\}$ of M are generic, i.e., points in F satisfy the following conditions:
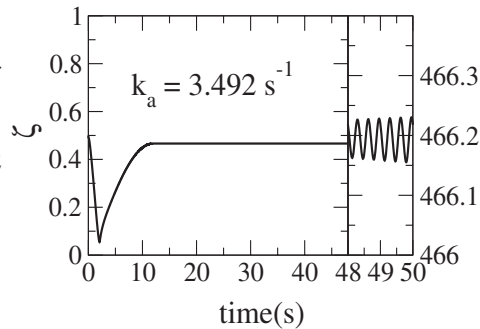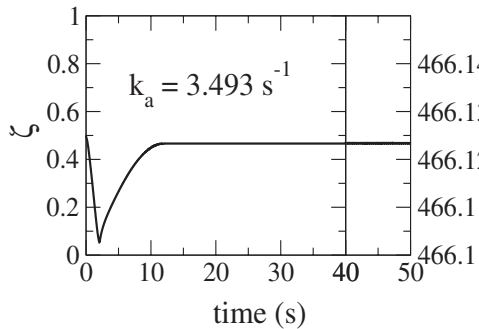

FIG. 10. Near the second transition, the system shows excitability of both the steady state before the Hopf bifurcation (left panel) and the small limit cycle after the Hopf bifurcation (right panel). Simulations are done for $v_g^{max} = 300$ nm s^{-1}; the time evolution of ζ is represented on two different scales (micrometers on the left, nanometers on the right).
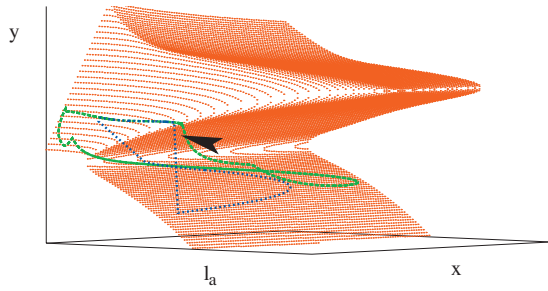
FIG. 11. (Color) Critical manifold M (red) and trajectory of the full (green) and reduced (blue) systems in the phase space (l_a-x-y) for $v_g^{max}=300$ nm s^{-1}, $k_a=3.482$ s^{-1}, and $\eta=10^{-3}$ pN s nm^{-1}. The upper and lower branches are attracting, the middle one is repelling. The only (unstable) steady state of the system is situated on the middle branch, near the fold, close to the point where both trajectories leave the upper branch (black arrow).

$$\frac{\partial^2 f_3}{\partial y^2} \neq 0, \quad \frac{\partial f_3}{\partial x} \neq 0, \quad \frac{\partial f_3}{\partial l_a} \neq 0, \quad f_1 \neq 0, \quad f_2 \neq 0.$$

The fold connecting lower and middle branches stays generic also for $k_a=k_a^C$.

(V) The only fixed point P [$f_1(P)=f_2(P)=f_3(P)=0$] of the problem is located close to one of the folds and switches from the upper attracting branch to the repelling branch when the attachment rate is reduced below k_a^C. At the critical value $k_a^C(0)$ this steady state becomes a nondegenerate canard point satisfying

$$\frac{\partial^2 f_3}{\partial y^2} \neq 0, \quad \frac{\partial f_3}{\partial x} \neq 0, \quad \frac{\partial f_3}{\partial l_a} \neq 0$$

and

$$\frac{\partial f_1}{\partial y} \neq 0, \quad \frac{\partial f_2}{\partial y} \neq 0, \quad \frac{\partial f_1}{\partial k_a} \neq 0, \quad \frac{\partial f_2}{\partial k_a} \neq 0.$$

Conditions I–V ensure [12] that for sufficient small η values, $k_a^H(\eta)$ and $k_a^C(\eta)$ exist, such that the following situations exist.

(1) For $k_a>k_a^H(\eta)$ a unique excitable stable state exists, that is situated on the upper attracting branch, close to the fold. If the system is slightly perturbed, it will return to its equilibrium immediately. Larger perturbations, beyond a well-defined threshold, will cause the system to make a big excursion before returning to equilibrium. The trajectory jumps from the upper branch to the lower branch, then moves close to the critical manifold toward the fold, jumps back to the upper branch when it comes to the fold, and finally moves on the upper branch towards the fold, being attracted by the steady state.

(2) For $k_a<k_a^H(\eta)$ a small stable limit cycle exists that appears through a supercritical Hopf bifurcation at $k_a=k_a^H(\eta)$. Similarly to the excitability of the steady state before the Hopf bifurcation, the small limit cycle is also excitable.

(3) For $k_a<k_a^C(\eta)$ a unique strongly attracting relaxation limit cycle exists. As shown in Fig. 11, the trajectory of this cycle remains close to the critical manifold M. When on one of the attracting branches, the system moves toward the fold.
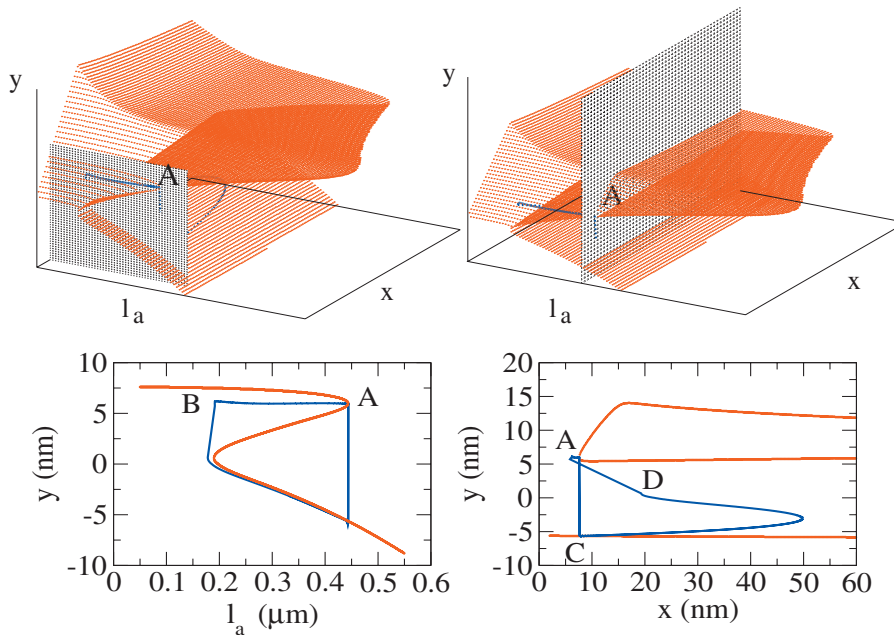

FIG. 12. (Color) Left: Section through the critical manifold M for $x=7.58$ nm (red) and the projection (blue) of the trajectory of the reduced system on the l_a-y plane. Right: Section through the manifold $\dot{y}=0$ for $l_a=443.72$ nm (red) and the projection (blue) of the trajectory of the reduced system on the x-y plane. The full three-dimensional trajectory crosses the represented sections in A. Between B and A the trajectory runs on the leaf of the manifold belonging to the upper branch. In A, the system leaves the manifold $\dot{y}=0$ and switches to the lower branch in C. Between C and D the trajectory runs on the lower leaf. From D to B, the system switches back from the lower to the upper attracting branch, going through the middle repelling branch.
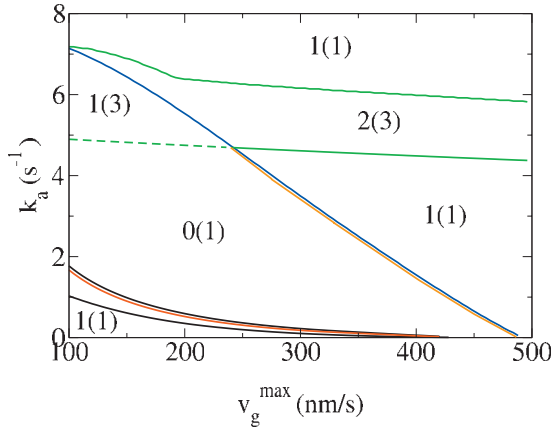
FIG. 13. (Color) Positions of the saddle-node bifurcations (black and green lines), homoclinic bifurcation (red line), Hopf bifurcation (blue line), and canard explosion (orange) in the parameter space v_g^{max}-k_a. Also displayed are the number of stable steady states and the total number of steady states (in parentheses) in the corresponding parameter domain. A second Hopf bifurcation exists very close to the lowest saddle-node bifurcation (lower black line) and is not shown here (see Figs. 8 and 14). Between the two black lines, there are three steady states, one being stable. Inside the oscillatory domain, the saddle node appears on the limit cycle (dashed green line).

When the fold is reached, the system leaves the critical manifold M and jumps almost instantaneously from one stable branch to the other one.

For comparison, the projection of the full system's trajectory and that of Eq. (2) on the (l_a, x, y) space are plotted in Fig. 11. Although there are considerable differences between the two cycles during motion on individual branches of the critical manifold M, the full system also follows M most of the time, switching between its attracting branches when it comes to a fold point. The transitions are smoother compared to the reduced system, suggesting that y is not the pure component corresponding to the fast time scale.

Figure 12 shows two-dimensional sections trough the manifold of Fig. 11 for fixed values of x (left) and l_a (right) and the projection of the trajectory of the reduced system on the l_a-y and x-y planes, respectively. We present the two sections that include the leaving point located close to the unstable steady state, where the trajectory of the reduced system leaves the upper attracting branch.

VI. BISTABILITY

We return now to the discussion of the bistable regime mentioned in Sec. III, where a stable stationary state coexists with the stable limit cycle. The results of the numerical simulations and of the linear stability analysis for the stationary states are summarized in Figs. 13 and 14. Figure 13 shows the different stability regimes in the v_g^{max}-k_a parameter plane. For a given value of v_g^{max}, the dependence of the steady states and their linear stability on k_a is represented in Fig. 14. As stated before, the lower transition line is located inside a region where one stable stationary state coexists with two
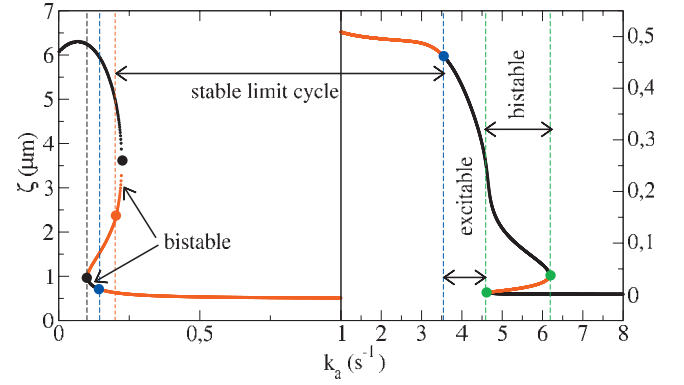

FIG. 14. (Color) Steady states and linear stability for v_g^{max} =300 nm s^{-1}. Stable states are shown with black, unstable ones with red lines. The points mark the saddle-node bifurcations (black and green), Hopf bifurcations (blue), and homoclinic bifurcation (red).

unstable ones and consists of the points where the cycle collides with one of the unstable points, giving rise to a homoclinic orbit (red point in Fig. 14). The bistable region, where the cycle coexists with one steady state is located between the red line and the upper black line. In addition to the transitions we already discussed, further bifurcations occur for attachment rates k_a that are larger than in the phase diagram of Fig. 3. Thus, another bistability region exists bounded by two saddle-node bifurcations at $k_a \approx 5$ s^{-1} and $k_a \approx 6$ s^{-1} (continuous green lines in Fig. 13). Here, two different stable steady states are found. For small values of the graft velocity v_g^{max} one of the steady states interferes with the oscillatory regime, and the canard explosion will not be observed. In this case, the oscillations disappear via a saddle-node bifurcation on the limit cycle (dashed green line in Fig. 13).

VII. CONCLUSIONS

We analyzed two different transitions from steady behavior to oscillations in a model for actin-based motility by varying the rate with which actin attaches to the obstacle. In the oscillatory regime, some of the physical quantities characterizing the system, such as the number and the pulling force of attached filaments, show short periods of very fast transition, resembling the temporal structure of relaxation oscillations. The small viscosity of the medium and the sensitive balance between pulling and pushing forces with comparable values and opposite signs introduce indeed a separation of the time scales: The position of the obstacle reacts very quickly compared to the other variables when the force balance changes. Since the fast variable position merely provides the transitions between the slow manifolds in the limit cycle, a decrease in the viscosity of the medium results in a saturation of the oscillation period at a nonzero value and not proportionality of the period to η.

A first transition from the oscillatory to a steady regime was shown to be preceded by bistability and occurs via a homoclinic bifurcation. The second transition occurs via a Hopf bifurcation. Short after this bifurcation, both period and

amplitude of the Hopf cycle increase suddenly as in a canard explosion. For a reduced three-dimensional system, obtained by a pseudo-steady-state approximation for one of the variables, we could indeed show the existence of a canard point. The reduced system is, however, only qualitatively a good approximation of the model, since the size and period of the cycle are considerably changed. Our system also shows excitability, a phenomenon that has been related to a canard explosion before.

We found a rich bifurcation scheme for the brush dynamics with our model. Such a variety has not been observed before. Only steady motion has been reported for the tethered ratchet model [24,31], which is a brush model similar to ours. Continuum models for the gel [11] show steady motion and oscillatory behavior if they are applied to curved obstacle surfaces. Here, we have shown that actin-based motility may indeed exhibit steady motion, excitability, bistability between attractors of different type, and oscillations. With such a survey we intended to reveal the possibilities hidden in brush dynamics beyond known experimental results. Hopefully, that will induce an experimental search for excitability and bistability. The existence of oscillations has been shown in experiments and we have offered an explanation by a push-pull mechanism derived from Eq. (1) [19].

Our model as presented here is for local brush dynamics and applies to plane rigid or pointlike obstacles. It can be extended to spatially extended soft obstacles, like the lamellipodium of crawling cells, especially since the existence of dynamic regimes does not require specific geometries. The leading edge of lamellipodia as recorded in experiments exhibits rich dynamics, including the repeated formation and retraction of membrane protrusions. It is likely that many of these events are controlled by some kind of stimulus and pathway. However, the action of a local perturbation of the shape of the leading edge on neighboring membrane regions will depend on the local dynamic regime of the leading edge. In both the excitable and bistable regimes, supercritical events will lead to singular waves in the shape of the leading edge. Similarly, wave phenomena in the oscillatory regime can cause periodic spatiotemporal structures as, for example, observed in [14,15].

Recent theoretical approaches to the leading edge problem [32,33] do not consider explicitly the dynamics of the brush of actin filaments, assuming that the obstacle velocity is the same as the growth velocity of the gel. This is true in the case of steady motion, when the brush reaches a stationary length distribution. However, precisely in the interesting case of an oscillatory movement, the obstacle and gel growth velocity are not equal. When the brush is buckled, the force on the obstacle is high, resulting in high obstacle velocity; at the same time, the high load reduces the polymerization velocity. By contrast, when the filament tips are far from the obstacle, the polymerization velocity is maximal, while the force on the obstacle and its velocity are minimal. Thus, for a general understanding of actin-based motility, the mechanics of the obstacle has to be separated from the dynamics of the actin gel growth. This implies the direct computation of the obstacle velocity from the balance of forces. For this, the dynamics of the length distribution of the brush has to be considered explicitly, as done in [19] and here.

The dynamic regimes found in this paper can be the basis for spatiotemporal structures in a spatially extended version of this model. That will be the subject of future work.

APPENDIX

We follow here the derivation of the model equations from [19]. Let $N_a(l,t)$ and $N_d(l,t)$ denote the length distributions of attached and detached filaments. Their time dynamics is described by

$$\partial_t N_a(l,t) = \partial_l(\tilde{v}_g N_a) + k_a N_d - k_d N_a,$$

$$\partial_t N_d(l,t) = \partial_l[(\tilde{v}_g - v_p)N_d] - k_a N_d + k_a N_a. \quad (A1)$$

The exchange between the attached and detached populations is given by attachment of detached filaments $k_a N_d$ and detachment of attached filaments $k_d N_a$. Shortening of the grafted end [velocity $\tilde{v}_g(l,\zeta) = v_g(l)\max(l/\zeta,1)$, see main text] and additional elongation of the free end (velocity v_p) for detached filaments induce only a shift of the distribution, described by the advection terms in (A1).

We define further the total numbers of attached and detached filaments:

$$n_a(t) \coloneqq \int_0^\infty N_a(l,t)dl, \quad n_d(t) \coloneqq \int_0^\infty N_d(l,t)dl,$$

and the mean lengths of attached and detached filaments,

$$l_a(t) \coloneqq \frac{1}{n_a}\int_0^\infty lN_a(l,t)dl, \quad l_d(t) \coloneqq \frac{1}{n_d}\int_0^\infty lN_d(l,t)dl.$$

Since $\tilde{v}_g \to 0$ for $l \to 0$ (see main text), and assuming $N_{a,d}(l,t) \to 0$ for $l \to \infty$ at all times t, we get further

$$\partial_t n_a = \int_0^\infty \partial_t N_a dl = k_a n_d - k_d n_a = -\partial_t n_d, \quad (A2)$$

$$\partial_t(n_a l_a) = \int_0^\infty l\partial_t N_a dl = \int_0^\infty \tilde{v}_g N_a dl + k_a l_d n_d - k_d l_a n_a,$$

$$\partial_t(n_d l_d) = \int_0^\infty l\partial_t N_d dl = \int_0^\infty (\tilde{v}_g - v_p)N_d dl + k_d l_a n_a - k_a l_d n_d. \quad (A3)$$

Inserting (A2) into (A3) and solving for $\partial_t l_a$ and $\partial_t l_d$ leads to

$$\partial_t l_a = \frac{1}{n_a}\int_0^\infty \tilde{v}_g N_a dl + k_a \frac{n_d}{n_a}(l_d - l_a),$$

$$\partial_t l_d = \frac{1}{n_d}\int_0^\infty (\tilde{v}_g - v_p)N_d dl + k_d \frac{n_a}{n_d}(l_a - l_d). \quad (A4)$$

For $\partial_t \zeta = 0$ and $k_a = 0$, the equation for $\partial_t N_d(l,t)$ can be solved exactly by the method of characteristics. As can be easily checked, all characteristics of the above equation converge to the equilibrium length l^*, at which growth of the free end by

polymerization balances shortening of the grafted end by cross linking:

$$\tilde{v}_g(l^*, \zeta) = v_p(l^*, \zeta).$$

This means we obtain

$$N_d(l,t) \rightarrow \int_{l_0^{\min}}^{l_0^{\max}} N_d(l',0)dl' \, \delta(l - l^*),$$

where $l_0^{\min}$ and $l_0^{\max}$ are the minimal and maximal lengths of the polymer at time $t=0$. As discussed in [19], the time scale of this contraction is in the range of less than 2 s for differences between l_a and l_d occurring during oscillations. That is fast compared to the typical period of oscillations. Motivated by this property, we make a monodisperse approximation also in the dynamic case $\partial_t \zeta \neq 0$, $k_a \neq 0$. We set

$$N_a(l,t) = n_a(t)\delta(l - l_a(t)), \quad N_d(l,t) = n_d(t)\delta(l - l_d(t)).$$

(A5)

Inserting Eq. (A5) into Eq. (A4) leads to

$$\partial_t l_a = \tilde{v}_g(l_a, \zeta) + k_a \frac{n_d}{n_a}(l_d - l_a),$$

$$\partial_t l_d = (\tilde{v}_g(l_d, \zeta) - v_p(l_d, \zeta))N_d dl + k_d \frac{n_a}{n_d}(l_a - l_d),$$

and we obtain further [see equation for $\partial_t \zeta$ in Eqs. (1)]

$$\int_0^\infty (N_a F_a + N_d F_d)dl = n_a F_a(l_a, \zeta) + n_d F_d(l_d, \zeta)$$

and

$$\frac{1}{N}\int_0^\infty v_g(l)(N_a(l,t) + N_d(l,t)) = \frac{n_a v_g(l_a) + n_d v_g(l_d)}{n_a + n_d}.$$

[1] T. Pollard, Nature (London) **422**, 741 (2003).
[2] R. Ananthakrishnan and A. Ehrlicher, Int. J. Biol. Sci. **3**, 303 (2007).
[3] M. Carlier and D. Pantaloni, J. Biol. Chem. **282**, 23005 (2007).
[4] Y. Marcy, J. Prost, M.-F. Carlier, and C. Sykes, Proc. Natl. Acad. Sci. U.S.A. **101**, 5992 (2004).
[5] A. Carlsson, Biophys. J. **81**, 1907 (2001).
[6] A. Carlsson, Biophys. J. **84**, 2907 (2003).
[7] M. Hamon, H. Bierne, and P. Cossart, Nat. Rev. Microbiol. **4**, 423 (2006).
[8] I. Lasa and P. Cossart, Trends Cell Biol. **6**, 109 (1996).
[9] E. Gouin, M. Welch, and P. Cossart, Curr. Opin. Microbiol. **8**, 35 (2005).
[10] I. Lasa, E. Gouin, M. Goethals, K. Vancompernolle, V. David, J. Vandekerckhove, and P. Cossart, EMBO J. **16**, 1531 (1997).
[11] F. Gerbal, P. Chaikin, Y. Rabin, and J. Prost, Biophys. J. **79**, 2259 (2000).
[12] M. Krupa and P. Szmolyan, J. Differ. Equations **174**, 312 (2001).
[13] H.-G. Döbereiner, B. J. Dubin-Thaler, G. Giannone, H. S. Xenias, and M. P. Sheetz, Phys. Rev. Lett. **93**, 108105 (2004).
[14] H.-G. Döbereiner, B. J. Dubin-Thaler, J. M. Hofman, H. S. Xenias, T. N. Sims, G. Giannone, M. L. Dustin, C. H. Wiggins, and M. P. Sheetz, Phys. Rev. Lett. **97**, 038102 (2006).
[15] M. Machacek and G. Danuser, Biophys. J. **90**, 1439 (2006).
[16] A. Upadhyaya and A. van Oudenaarden, Curr. Biol. **13**, R724 (2003).
[17] A. Upadhyaya and A. van Oudenaarden, Curr. Biol. **14**, R467 (2004).
[18] A. Bernheim-Groswasser, J. Prost, and C. Sykes, Biophys. J. **89**, 1411 (2005).
[19] A. Gholami, M. Falcke, and E. Frey, New J. Phys. **10**, 033022 (2008).
[20] C. Co, D. Wong, S. Gierke, V. Chang, and J. Taunton, Cell **128**, 901 (2007).
[21] T. Svitkina, Cell **128**, 828 (2007).
[22] E. Evans and K. Ritchie, Biophys. J. **72**, 1541 (1997).
[23] K. Kroy and E. Frey, Phys. Rev. Lett. **77**, 306 (1996).
[24] A. Mogilner and G. Oster, Biophys. J. **71**, 3030 (1996).
[25] A. Gholami, J. Wilhelm, and E. Frey, Phys. Rev. E **74**, 041803 (2006).
[26] S. Wiesner, E. Helfer, D. Didry, G. Ducouret, F. Lafuma, M. Carlier, and D. Pantaloni, J. Cell Biol. **160**, 387 (2003).
[27] L. Trichet, O. Campàs, and C. Sykes, Biophys. J. **92**, 1081 (2007).
[28] M. Brøns and J. Sturis, Phys. Rev. E **64**, 026209 (2001).
[29] B. Deng, Chaos **14**, 1083 (2004).
[30] M. Brøns and K. Bar-Eli, J. Phys. Chem. **95**, 8706 (1991).
[31] A. Mogilner and G. Oster, Biophys. J. **84**, 1591 (2003).
[32] R. Shlomovitz and N. S. Gov, Phys. Rev. Lett. **98**, 168103 (2007).
[33] K. Kruse, J. Joanny, F. Jülicher, and J. Prost, Phys. Biol. **3**, 130 (2006).